Photoacoustics 24 (2021) 100305

Contents lists available at ScienceDirect

Photoacoustics

journal homepage: www.elsevier.com/locate/pacs

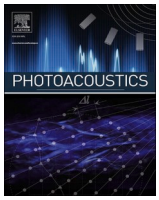

Broadband surface plasmon resonance sensor for fast spectroscopic photoacoustic microscopy

Fan Yang, Guangdi Guo, Shanguang Zheng, Hui Fang, Changjun Min, Wei Song *, Xiaocong Yuan *

Nanophotonics Research Center, Shenzhen Key Laboratory of Micro-Scale Optical Information Technology, Institute of Microscale Optoelectronics, Shenzhen University, Shenzhen, 518060, China

ARTICLE INFO

Keywords:
Surface plasmon resonance
Broad bandwidth
Photoacoustic microscopy
Photoacoustic spectroscopic analysis
High-speed imaging

ABSTRACT

High-speed optical-resolution photoacoustic microscopy (OR-PAM), integrating the merits of high spatial resolution and fast imaging acquisition, can observe dynamic processes of the optical absorption-based molecular specificities. However, it remains challenging for the evaluation to morphological and physiological parameters that are closely associated with photoacoustic spectrum due to the inadequate ultrasonic frequency response of the routinely-employed piezoelectric transducer. By utilizing the galvanometer for fast optical scanning and our previously-developed surface plasmon resonance sensor as an unfocused broadband ultrasonic detector, high-speed spectroscopic photoacoustic imaging was accessed in the OR-PAM system, achieving an acoustic bandwidth of ~125 MHz and B-scan rate at ~200 Hz over a scanning range of ~0.5 mm. Our system demonstrated the dynamic imaging of the moving phantoms' structures and the simultaneous characterization of their photoacoustic spectra over time. Further, fast volumetric imaging and spectroscopic analysis of microanatomic features of a zebrafish eye ex vivo was obtained label-freely.

1. Introduction

Photoacoustic (PA) imaging technology, detecting ultrasounds generated from laser pulse absorption of biomolecules, provides optical absorption contrasts for structural, functional, and molecular imaging [1–3]. Over the past decades, the technology has found broad applications in investigating the physiopathology processes, for example imaging subcutaneous microvasculature, early diagnosis of tumors, and monitoring the blood oxygenation [4–14]. Among various PA imaging techniques, optical-resolution photoacoustic microscopy (OR-PAM), applying optical objective for focusing the illumination laser, achieves diffraction-limited lateral resolution down to micrometer scale and even sub-micrometers, which thus reveals the optical absorption properties of the biological tissue at cellular level and even subcellular level [15,16]. Moreover, by the utilization of fast scanning mechanisms (e.g., galvanometer scanner or microelectromechanical system), the OR-PAM system accesses high-speed imaging acquisition, allowing for monitoring the dynamic physiological processes with mitigated motion artifacts [17–20].

For PA imaging acquisition, the signal amplitude is proportional to the optical absorption coefficient and local optical fluence, contributing to map the optical absorption distribution within the biological samples [1–3]. In addition to providing one dimensional depth-resolved information, intrinsic acoustic spectra in the PA impulses are closely associated to the microscopic orientation of the biological samples [1,2]. Therefore, analyzing the PA signals in the frequency domain offers the opportunities for quantitative evaluation on the microscopic features of biological particles stochastically distributed in tissues, including size, shape, orientation, and density [24]. Since the characteristic scale of various biological particles ranges from over 100 micrometers (e.g., blood vessels or lipid clusters) to the order of a few micrometers or submicron (e.g., individual red blood cells or cellular nuclei), the corresponding PA waves possess a very broad acoustic spectral band (from nearly DC up to ~hundreds of megahertz). This, thus, requires the ultrasonic detector with sufficient acoustic frequency response. Unfortunately, the piezoelectric transducers routinely used in the most existing PA imaging setups generally operate over a relatively narrow bandwidth (centered at its resonance frequency) because of the inherent physical property of the piezoelectric material [21–24]. In consequence, it inevitably imposes difficulties for acquiring broadband PA waves using

* Corresponding authors.
E-mail addresses: weisong@szu.edu.cn (W. Song), xcyuan@szu.edu.cn (X. Yuan).

https://doi.org/10.1016/j.pacs.2021.100305
Received 4 June 2021; Received in revised form 16 August 2021; Accepted 15 September 2021
Available online 21 September 2021
2213-5979/© 2021 The Authors. Published by Elsevier GmbH. This is an open access article under the CC BY-NC-ND license (http://creativecommons.org/licenses/by-nc-nd/4.0/).

the traditional piezoelectric transducers. This might overlook the abundant morphological information within the biological tissues [22,23].

To overcome the drawbacks arising from the piezoelectric transducers, optical detection approaches of the ultrasounds have been proposed for the PA measurement [25–32]. Fabry–Perot interferometer can detect the ultrasounds with enhanced sensitivity, whereas its frequency response less than 50 MHz exacerbates the axial resolution and the PA volumetric imaging is still compromised [27]. The imprinted polymer optical micro-ring resonator possesses superior detection bandwidth with high ultrasonic detection sensitivity and large field of view (FOV) [25,26]. However, the detector requires time-consuming fabrication procedures with low yield, possibly imposing severe difficulties in practical biomedical PA applications. Taking advantage of ultrafast temporal response and strongly localized evanescent field at the interface of the sensing material and coupling medium, optical surface wave sensing technology, such as surface plasmon resonance (SPR) sensor [28], polarization dependent reflection ultrasonic detection (PRUD) [29], and graphene-based detector [30], emerges as a promising candidate for the ultrasonic detection. Strikingly, by applying the polarization-differential light detection approach, our recently-developed SPR sensor can detect the PA impulses with high sensitivity over a broad acoustic spectral range (>170 MHz) [31,32]. This potentially enables the accurate response to the pressure transients from the biological specimens.

In this work, we developed a fast spectroscopic OR-PAM system for dynamic imaging and spectroscopic analysis of the moving objects, where a broadband SPR sensor maintained stationary for wide-directivity PA signal detection and a galvanometer was used for high-speed optical raster scanning. The directional response to the pressure transients of our SPR sensor was studied both theoretically and experimentally, which defined the OR-PAM system's FOV at ~0.37 mm (x) × ~0.74 mm (y) for the axial distance at ~0.6 mm. High-speed B-scan imaging acquisition at ~200 Hz was achieved over a scanning range of ~500 μm with ~4.7-μm lateral resolution and ~125-MHz frequency response. We demonstrated the system's feasibility for monitoring the movement of the phantoms and simultaneously characterizing the dynamics of the PA spectra. Further, label-free volumetric imaging of a zebrafish eye *ex vivo* was performed, which enabled the spectroscopic analysis of its microanatomic structures.

2. Methods

2.1. Working principle of the SPR sensor

Fig. 1(a) shows the schematic diagram of the high-speed spectroscopic PA imaging module, where an SPR sensor remains stationary for broadband ultrasonic detection and a galvanometer is employed for the fast raster scanning. For the PA excitation, a laser beam with high pulse repetition frequency (PRF) was redirected by a two-dimension galvanometer, and then focused on the sample by an objective, which realizes the optical raster scanning for fast PA imaging acquisition [17]. Our previously-developed SPR sensor acts as an unfocused ultrasonic detector, allowing for measuring the PA signals with broad bandwidth and wide directivity [31,32].

Based on the theory of electromagnetic wave propagation in a stratified conductive medium, surface plasmon polaritons are excited for the p-polarized incident light at certain incident angles (i.e., satisfying the wavenumber matching condition) [33]. This accompanies a declined light reflectance (Fig. 1(b)) because a fraction of the incident light energy is transferred to the surface plasmon polaritons. The optimum incident angle of the SPR sensor (labeled by the red line) is studied theoretically in Fig. 1(b). During the PA detection, the SPR sensor's signal output was obtained by recording the intensity variation of the reflected light rather than the reflectivity [28–32]. For each incident angle (θ), the light intensity of the reflected beam (I_R) delivered to the photodiode was carefully adjusted to avoid the power saturation of the photodiode (~0.225 mW in this work). The optimum incident angle can be derived by seeking the maximum of the first derivative of the reflected light intensity with respect to the incident angle (i.e., $|dI_R/d\theta|$),

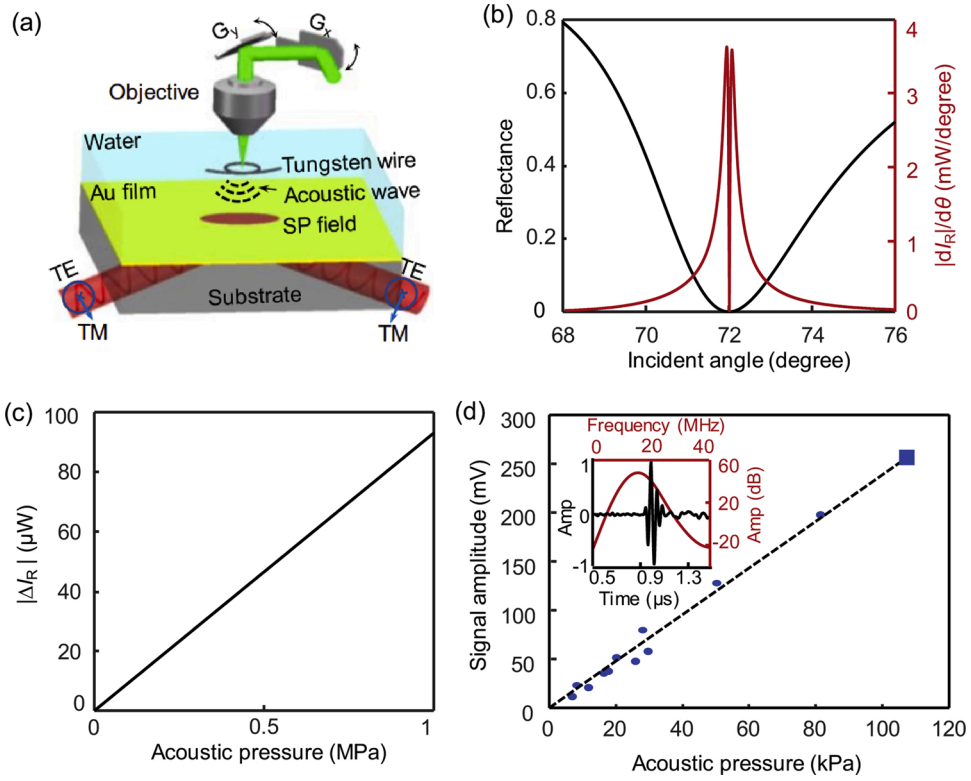

Fig. 1. Working principle of the SPR sensor. (a) Schematic of wide-directivity PA detection by a stationary SPR sensor and fast-scanning galvanometer. Gx and Gy: two mirrors of the galvanometer; TE: transverse electric field; TM: transverse magnetic field. (b) Determination of the optimum incident angle. The dark line presents the reflectance (R) as a function of the incident angle (θ); the red line exhibits the first derivative of the reflected light intensity with respect to the incident angle (|dIR/dθ|), where IR is defined as the intensity of the reflected light for the incident angle at θ. (c) The intensity variation of the reflected light (|ΔIR|) with respect to acoustic pressure, where the intensity difference (ΔIR) denotes the pressure-modulated value relative to that under static conditions. (d) Pressure response of the SPR sensor for the ultrasonic excitation. The inset shows the ultrasonic waveform and spectrum detected by the SPR sensor when the acoustic pressure is at ~107.0 kPa (highlighted by a blue box). Amp: amplitude.

determining the optimum incident angle of our SPR sensor at ~71.9 ° in Fig. 1(b).

During the PA detection, the laser-induced acoustic pressure (Δp) causes the variation in refractive index (RI) of the water (Δn) (following a relationship of $\Delta n/\Delta p \approx 1.35 \times 10^{-10} Pa^{-1}$ [30]). This leads to the changes in the reflected light intensity ($|\Delta I_R|$) relative to the value under initially static water when the incident angle is fixed at ~71.9 °. In Fig. 1 (c), $|\Delta I_R|$ displays a linear dependence upon the acoustic pressure with a slope ($K = |\Delta I_R|/\Delta p$) of ~$9.3 \times 10^{-5}$ μW/Pa. The minimum detectable acoustic pressure (P_{min}) of our SPR sensor can be expressed as

$$P_{min} = \frac{R_{noise}}{K} \tag{1}$$

where R_{noise} represents the BP's the noise level (μW) that primarily determines the minimum differentiable light energy variation. Considering the photoelectric conversion gain of ~16×10^3 V/W and the electrical noise of ~0.18 mV of the BP, the noise level is estimated at ~0.01125 μW. Thus, the minimum detectable acoustic pressure of our SPR sensor is quantified at ~121 Pa. Note that the simulation in Fig. 1(c) suggests the pressure dynamic range of the SPR sensor at least ~1 MPa in theory, much larger than the pressure values in practical biomedical PA imaging [2].

We measure the detection sensitivity of our SPR sensor in Fig. 1(d). An acoustic emission source from a piezoelectric transducer (Olympus, ~20-MHz central frequency) driven by a pulse receiver (Olympus, 5073PR) was pre-calibrated by a commercial hydrophone (HGL-0085, Onda Corp.). Ultrasounds caused the changes in the water RI, resulting in the temporary modulations to the light reflectance in the SPR sensor [31,32]. Both waveform and spectrum captured by our SPR sensor (the inset of Fig. 1(d)) resembled the pulse echo detected with the piezoelectric transducer (not shown), suggesting the accurate response to the ultrasonic excitation of our SPR [31,32]. The peak value of the SPR sensor's signal output is approximately linear with respect to the acoustic pressure (ranging from ~3.0–107.0 kPa) in Fig. 1(d). By extrapolating the linear range down to the noise level, we estimated the sensor's noise-equivalent-pressure sensitivity at ~480 Pa. The SPR sensor's sensitivity determined experimentally is remarkably worse than the theoretical value (Fig. 1(c)), which is possibly from the imperfections in the sensor configuration, such as uneven illumination on the two separate photodetectors of the BP, the non-parallel interrogation light on the Au layer (i.e., the incident laser beam with a diverging angle), and the rough Au film surface.

2.2. Directional response of the SPR sensor

To access high-speed PAM imaging, the SPR sensor, serving as an unfocused ultrasonic detector, remains stationary during the imaging while the galvanometer operates at fast raster scanning of the PA illumination laser (Fig. 1(a)). Thus, it is required to study the directional acoustic response of our SPR sensor for determine the OR-PAM system's FOV. The theoretical study on the directional response of our SPR sensor to the ultrasonic waves is conducted in Fig. 2. The surface plasmon (SP) field is reasonably identified as an active acoustic detection element [34]. Theoretically, the detected acoustic pressure of an SPR sensor is equivalent to the pressure value generated from a region that has an identical area with the SP field of the sensor. Owing to the extremely short penetration depth of highly localized evanescent SP waves, the SP field's thickness is neglected [31,32].

In the theoretical analysis, the SP field is assumed as elliptical with the long axis of ~180 μm and the short axis of ~90 μm, respectively, which is approximated to the lateral dimensions in our home-made SPR sensor. The *x*-*y* plane of the coordinate system (Fig. 2(a)) coincides with the Au-water interface, in which the origin locates at the center of the SP field and the *y* axis parallels to its long axis. The spherical acoustic waves emitting from an excited point source located at *A* (*x*, *y*, *z*) propagate through coupling medium to perturb the SP field, changing the reflectance of the SPR sensor. The continuous acoustic waves in the form of the time harmonic are expressed by

$$u = u_0 e^{-j\omega t} \tag{2}$$

where u_0 is the ultrasonic source vibration amplitude and ω is the ultrasonic angular frequency. The amplitude of the detected pressure can be calculated as [35,36]

$$|p(x,\ y,\ z,t)| = \frac{\omega \rho_0 u_0}{2\pi} \left| \int \frac{e^{-jkR}}{R} dS \right| \tag{3}$$

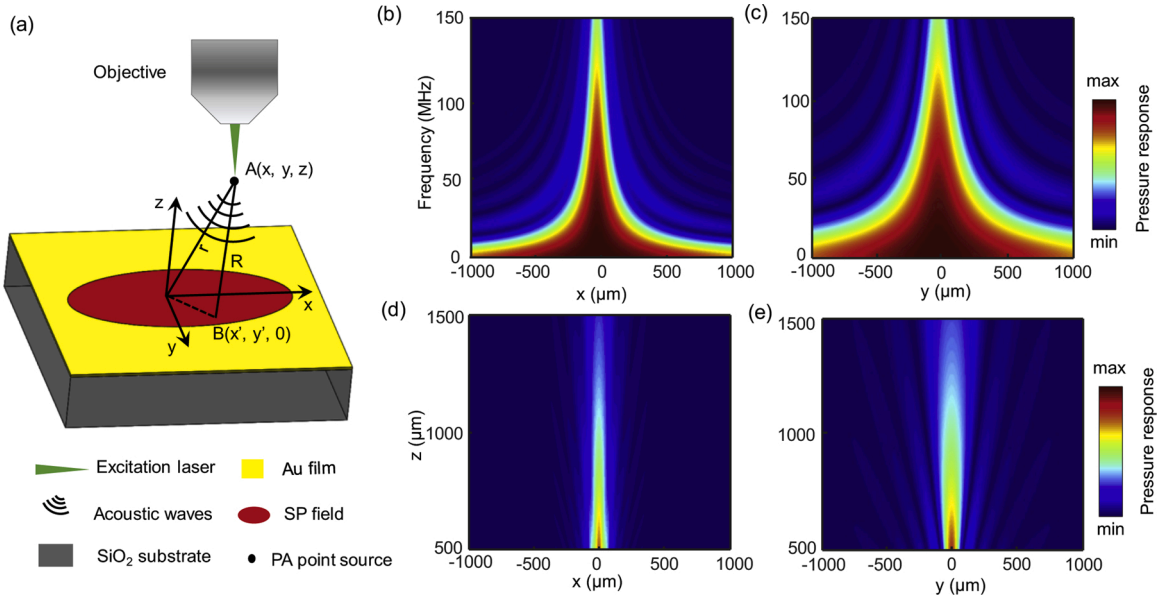

Fig. 2. Directional response characteristics of the SPR sensor. (a) Schematic of an SPR sensor and its response to acoustic source. A (x, y, z) and B (x', y', 0) are the positions of the acoustic source and the representative detection point of the SP field, respectively; R is the distance from the source to the detection point. (b) and (c) present the SPR sensor's frequency response at x-z plane (b) and y-z plane (c), respectively, for the working distance at 1.0 mm. (d) and (e) show the distance-dependence ultrasonic response of the SPR sensor at x-z plane (d) and y-z plane (e), respectively, for the ultrasonic frequency at 100 MHz.

where p is the detected pressure, ρ_0 is the conversion factor from acoustic pressure to voltage by our SPR sensor, and k is the ultrasonic wave vector. R is the distance from the acoustic source to a certain point (B (x', y', 0)) of the SP field, which can be expressed as $R = \sqrt{(x-x')^2 + (y-y')^2 + z^2}$ according to the geometrical relationship in Fig. 2(a). Integral domain S represents the lateral dimension of the SP field. Due to proportional relation between the amplitude of a monopole acoustic source and its frequency, we remove the frequency term ω from Eq. (3) to unify the acoustic amplitude at different frequencies [35]. The SPR sensor's response to the ultrasonic waves is given as below:

$$|p'(x,\ y,\ z,t)| = \frac{\rho_0 u_0}{2\pi}\left|\int \frac{e^{-jkR}}{R} dS\right| \quad (4)$$

Taking into account of the acoustic attenuation (2.2×10^{-4} dB/mm^{-1}/MHz^{-2}) in the water, the frequency response patterns of the SPR sensor are characterized in Fig. 2(b) and (c) when the working distance is set at 1000 μm. In both axes, the trend in the ultrasonic response at certain frequency appears similar, in which the pressure values decline as the lateral distance relative to the SPR sensor's detection axis increasing. This feature becomes more serious for the high-frequency ultrasonic waves. Note that the directional response range along x axis and y axis is different owing to the asymmetric characteristics in the SP field of the SPR sensor [36].

Besides, we study the working distance-dependent ultrasonic response of the SPR sensor in Fig. 2(d) and (e). Here, the ultrasonic frequency is intentionally set at 100 MHz because it is in close proximity to the central frequency of acoustic spectral band of our SPR sensor itself [32]. For a given axial position, strong pressure response is in the close proximity to the center of the SPR sensor's SP field. As the lateral distance between the point acoustic source and the SPR sensor increasing, the pressure response degrades at both x-z plane (Fig. 2(d)) and y-z plane (Fig. 2(e)). At larger axial distance, a weaker pressure response occurs. Due to an asymmetric feature of the SPR sensor's SP field, the spatial response exhibits the different patterns at the two planes (Fig. 2(d) and (e)) [30]. The theoretical simulations on the directional response characteristics of our SPR sensor (Fig. 2) allow for guiding the FOV design in the OR-PAM system [19,20].

2.3. PA spectral calibration

The time-resolved PA signal is produced by focusing the pulse laser onto the ultrathin graphene film with the thickness of ~100 nm [31,32], giving the PA spectrum from its Fourier transform. The frequency response of the measured PA signal (f_{PA}) can be expressed as the product of our OR-PAM system's frequency response (f_{sys}) and the original PA spectrum of the sample (f_{sam}). Since the acoustic transient time crossing the graphene film is far shorter than the laser pulse duration (~1.2 ns), the sample's PA spectrum (f_{sam}) is essentially identical to the power spectrum of the illuminating laser (f_{laser}). Therefore, the frequency response of our OR-PAM itself can be derived from $f_{sys}=f_{PA}/f_{laser}$. For the spectroscopic analysis of the samples, the autologous spectrum (f_{sam}) can be derived from $f_{sam}=f_s/f_{sys}$ according to their measured PA spectra (f_s) and the pre-calibrated frequency response of the system (f_{sys}).

3. Results and discussion

3.1. Development of fast spectroscopic OR-PAM system

Fig. 3(a) shows the schematic of the high-speed spectroscopic OR-PAM system. Our recently-built SPR sensor was incorporated into the system as a broadband acoustic detector [31,32]. In brief, an interrogation light from a He – Ne laser (HNL100L-EC, Thorlabs Inc., 632.8-nm wavelength) passes through a polarizer (P, LPVISE100-A, Thorlabs Inc.) and a half-wavelength plate (HWP, WPH10M-633, Thorlabs Inc.), producing a tunable linearly polarized light. After weakly focused by an achromatic lens (L_1), the interrogation light is incident onto the

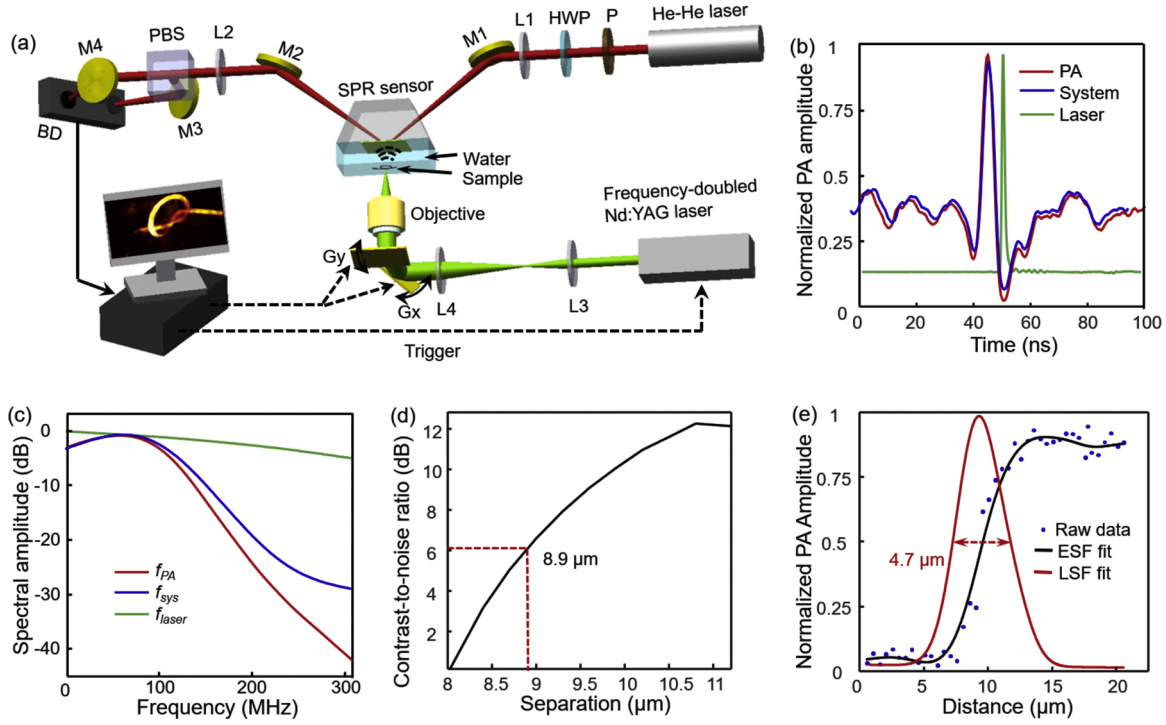

Fig. 3. (a) Schematic of the high-speed spectroscopic OR-PAM system. P: polarizer; HWP: half-wave plate; L: lens; M: mirror; PBS: polarization beam splitter; BP: balanced photodiode; Gx and Gy: two mirrors of the galvanometer. (b) Temporal profiles of the pulse laser, measured PA signal, and the system itself. (c) Spectra of the pulse laser (flaser), the measured PA signal (fPA), and the system (fsys). (d) Depth resolution determined by the numerical shift-and-sum simulation. (e) The OR-PAM system's lateral resolution.

prism-water interface with an incident angle at ~71.9 ° (Fig. 1(b)). For configuring the SPR sensor for PA imaging, Au film is preferred because it is immunized from oxidization in both the air and water, which assures excellent stability during the practical biomedical PA applications. An SP field is excited on the Au film surface, featuring approximately elliptical structure [31,32]. Polarization-differential light detection is adopted for reducing the noises [29–32], which applies a polarization beam splitter (PBS, CCM1-PBS251, Thorlabs Inc) for separating the linearly-polarized reflected beam into *p*- and *s*-polarized components and a BP (PDB435a, Thorlabs Inc) for the light intensity measurement. Eventually, a broadband PA wave is retrieved by measuring the intensity difference between the time-varying *p*-polarized light and the invariant *s*-polarized light [29–32]. The SPR sensor's signal output is amplified by a low-noise amplifier (ZFL500NL+, Mini-Circuits, Brooklyn, NY) and digitized by a data acquisition card (ATS9870, Alazar Technologies Inc., Pointe-Claire, QC, Canada; 450-MHz bandwidth, 1-GS/s sampling rate).

For high-speed PA imaging, a galvanometer (TSH8203 M, Sunny) is employed for the raster scanning while maintaining both the SPR sensor and sample stationary during the PA signal acquisition. The PA illumination beam from a frequency-doubled Nd: YAG laser (SPOT-532, Elforlight Ltd., Daventry, UK.) is collimated by a pair of lenses (L_3 and L_4 in Fig. 3(a)), and then is redirected by the galvanometer. An objective (RMS4X, Olympus;) with numerical aperture (NA) of 0.1 is used to focus the PA illumination beam with a micrometer-level spot size on the sample [30]. This is much smaller compared with the SP field's lateral dimension, indicating that the ultrasonic emission from a point source is reasonable in the theoretical analysis (Fig. 2). An interconnect card (PCIe-6321, National Instruments) programmed in LabVIEW is used to synchronize the excitation laser firing, raster scanning, and data acquisition.

We study the PA response of the OR-PAM system by irradiating a layer of graphene film (~100 nm in thickness) in Fig. 3(b). Broadband PA waves can be produced by focusing the pulse laser beam onto the ultrathin optical-absorption sample [31,32]. The time-resolved PA signal was recorded with a digital oscilloscope (MDO3104, Tektronix; bandwidth: 1 GHz; sampling rate: 5 GS/s) in Fig. 3(b), which corresponds to the power spectrum (f_{PA}) with a bandwidth of ~125 MHz in Fig. 3(c). The frequency response of our OR-PAM itself (f_{sys}) can be derived from $f_{sys}=f_{PA}/f_{laser}$, where f_{laser} is the spectrum (Fig. 3(c)) of the PA illumination laser pulse (Fig. 3(b)). This indicates that our OR-PAM system possesses an estimated bandwidth of ~130 MHz in Fig. 3(c). The corresponding signal waveform at the time domain is exhibited in Fig. 3 (b). For the PA spectral analysis of the phantoms and biological tissues, the frequency characteristics of the samples itself (f_{sam}) can be calculated from $f_{sam}=f_s/f_{sys}$, where f_s represents the measured spectral response using our OR-PAM system. Considering the SP field's lateral dimensions of our SPR sensor and the distance (~1.0 mm) between the graphene film and the sensor surface, the measured spectral bandwidth is in accordance with the theoretical results [36]. Note that our OR-PAM system is sufficient for the PA imaging of biological tissues because the ultrasound attenuates seriously within tissues as the frequency more than 100 MHz [37,38].

During the PA imaging, the axial (depth) resolution (R_a) depends upon the sound speed (c) and the detector's bandwidth (BW) [30], which is expressed as $R_a = 0.88c/BW$. Thus, the axial resolution in our OR-PAM system incorporating an SPR sensor is estimated at ~10.4 μm. Alternatively, the resolving capability along the depth direction can be quantified by numerical shift-and-sum simulation [39,40]. Assuming two optical-absorption point absorbers that produce the same PA impulses (as displayed in Fig. 3(b)) are positioned at different depth separations, the time-shifted waveform for two PA impulses defines the axial resolution at ~8.9 μm when the contrast-to-noise ratio decreasing to 6.0 dB (Fig. 3(d)). This agrees with the estimated value (~10.4 μm) that is predominately determined by the sensor's bandwidth. In addition, benefiting from the broadband frequency response of the SPR sensor, a more accurate evaluation is potentially accessed for the PA spectroscopic analysis of the biological specimens with various dimensions [36], which, otherwise, is impossible for the PAM systems with the traditional piezoelectric transducers due to the inadequate acoustic spectral response [24].

The lateral resolution of our system is quantified in Fig. 3(e). A sharp blade edge was imaged using the PA illumination with 50-nJ pulse energy and ~100-nm scanning step. PA amplitudes across the edge gave the edge spread function (ESF, Fig. 3(e)). Taking the first derivative of the ESF, a line spread function (LSF) was derived to define the lateral resolution of ~4.7 μm (Fig. 3(e)) [41]. Due to optical aberrations at the air-water interface, the estimated lateral resolution was slightly worse than the theoretical diffraction-limited resolution. Obviously, the PA illumination focus spot on the sample is much smaller than the SP field's dimension (having an elliptical structure with ~90-μm short axis and ~180-μm long axis). Therefore, it is reasonable for considering the ultrasonic wave emission from a point source (Fig. 2) because of the PA excitation volume with a micrometer-scale lateral dimension and nanometer-level vertical length.

3.2. FOV determination of the OR-PAM system

The OR-PAM system's FOV, which is primarily dependent on the directional response of the acoustic detector, is critical for denoting the imaging region [35,36]. In Fig. 4, the FOV is determined by imaging a black tape, which was mounted on an one-dimensional stage for adjusting its axial distance relative to the sensor while the PA illumination focus maintained on the sample at each axial distance. During the PAM imaging at each distance, both the SPR sensor and the sample remained stationary, and only galvanometer was activated for the raster scanning. A volumetric image consisting of 300 pixels (x) × 300 pixels (y) × 512 pixels (z) was acquired by setting the laser PRF at 30 kHz and the scanning step at 10 μm, which took ~0.01 s for the B-scan imaging (i.e., 100-Hz B-scan rate) and ~3.0 s for the whole three-dimensional imaging. We applied the PA illumination with the pulse energy at ~80 nJ, which induced no obvious damage to the sample. A representative maximum-amplitude-projection (MAP) image by projecting the maximum PA amplitude of each A-line along the depth direction is displayed in Fig. 4(a), where the sample was positioned ~0.6 mm away from the SPR sensor. The PA amplitudes along x axis and y axis (highlighted by the blue and dark dashed lines in Fig. 4(a), respectively) are shown in Fig. 4(b), indicating the estimated FOVs at ~0.34 mm and ~0.76 mm along these two directions according to the full width at half maximum (FWHM) of the fitting curves. The remarkable difference in the FOVs at x axis and y axis primarily arises from the elliptical SP field of the SPR sensor [34], representing a good agreement with the theoretical result (Fig. 2).

As the axial distance increases, the OR-PAM system's FOVs enlarges as illustrated in Fig. 4(c). The distance-dependence characteristic of the FOV is in accordance with the simulations (dashed lines in Fig. 4(c) and Fig. 2(d) and (e)). Although an enlarged FOV can be achieved when positioning the sample at a larger axial distance (Fig. 4(c)), the frequency response of the system is compromised as the transverse displacement of the PA illumination spot relative to the SPR sensor's acoustic detection axis increasing (Fig. 2(b–e)) [36]. When performing the PA imaging of the large-scale specimens (e.g., major blood vessels), they can be placed at a relatively distant axial position because the frequency components of their PA signals are dominated at the low-frequency ranges [23,24]. For PAM imaging of the biological particles with small dimensions (e.g., red blood cells or cell nuclei) that launches the PA impulses with broad acoustic spectrum up to hundreds of megahertz, a reduced axial distance is preferred to ensure the accurate response to high acoustic frequency [21,22].

3.3. Fast spectroscopic imaging of the phantom

We performed the spectroscopic imaging of a moving phantom made

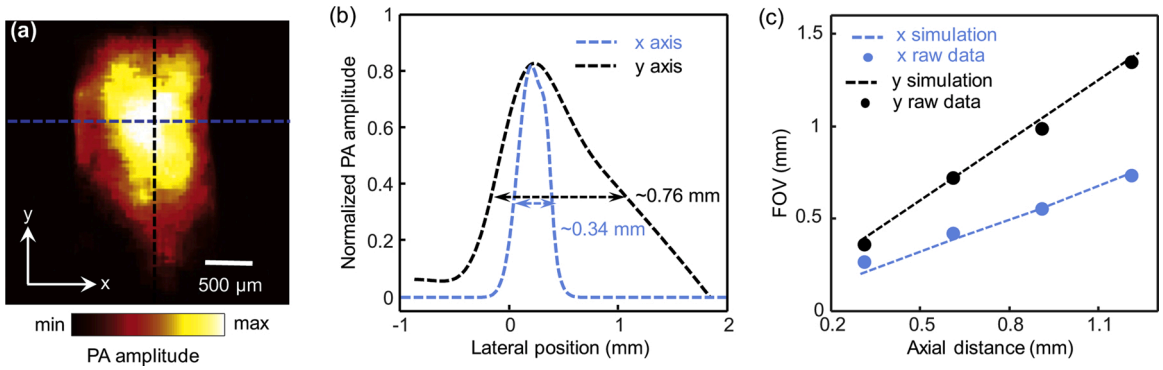

Fig. 4. Determination of our OR-PAM system's FOV. (a) PAM MAP image of a black tape that is positioned ~0.6 mm away from the sensor surface, defining the FOV (b) along x axis and y axis, respectively. (c) Estimation of the FOVs at different axial distances.

from a piece of black tape that was transversely translated (MT1/M-Z8, Thorlabs Inc.) with an averaged velocity of ~0.045 mm/s. The FOV of the OR-PAM system was set at an area of 750 μm × 750 μm (Fig. 5(a)), which consumed ~0.75 s per frame for acquiring a volumetric image consisting of 150 pixels (x) × 150 pixels (y) × 512 pixels (z) when adopting the PA illumination at 30-kHz PRF and ~5.0-μm scanning step size. Sequential PAM images were captured as the phantom crossing through the system's FOV (Fig. 5(a) and Video 1 in Supplementary file). At each snapshot, time-resolved PA signals were selected from 50 pixels of the sample. The acoustic spectra (f_s) were readily derived by the Fourier transformation to these PA signals. After recovering the original spectra of the phantoms according to $f_{sam}=f_s/f_{sys}$ and averaging the normalized acoustic spectra, the PA frequency response of our OR-PAM at each frame was characterized. Fig. 5(b) represents the measured bandwidths (-6.0 dB) of the PA spectra over time. As expected, only a slight fluctuation (17.2 MHz ± 1.8 MHz) in the spectral band appeared frame by frame because of the same sample imaged during the whole period. The relatively narrow spectral bandwidth of the phantom is attributed to the fact that the black tape itself with the large thickness (~180 μm) produces the PA impulses with dominant low frequency components [31], even though the broadband frequency response of our SPR sensor (Fig. 3(c)). Potentially, our OR-PAM system could not only visualize the moving large-dimension biological specimens (e.g., the cell aggregations in the major blood vessels) [45] but conduct the PA spectroscopic analysis to these objects.

Further, a complicated phantom made from a tungsten filament knot (40 μm in diameter) is imaged in Fig. 6 using our high-speed spectroscopic OR-PAM system. Because the tungsten filament has strong optical absorption with very shallow optical penetration depth at visible light range [32], broadband PA waves can be produced under the illumination of 532-nm wavelength. A home-made mount with a window (Fig. 6(a)) was used to hold the tungsten filament knot for both the PA illumination and the acoustic coupling, and then was transferred to an one-dimensional motorized stage. The galvanometer mirrors were activated for fast raster scanning, which covered the imaging region with an area of 50 μm (x) ×500 μm (y) (Fig. 6(b)). The number of scanning points at each B-scan (along y axis) was 100, corresponding to the B-scan rate of 200 Hz by setting the laser PRF at 20 kHz. Due to the limited directional response along x axis of our SPR sensor (Fig. 2 and 4), we intentionally reduced the scanning region at the x direction for adequate PA detection. Thus, the three-dimensional imaging acquisition took 0.05 s for each snapshot. Once the raster scanning was completed, the one-dimensional motorized stage was synchronized for moving the phantom towards the FOV of our SPR sensor with a step size of 50 μm. The fast raster scanning of the galvanometer and the mechanical scanning of motorized stage operated sequentially until the phantom was imaged completely. It took ~1.0 s for acquiring the whole phantom imaging (Fig. 6(c)) with an area of 1000 μm (x) ×500 μm (y), much faster compared with the previously-developed OR-PAM systems using the mechanical raster scanning [31,32]. More importantly, the delicately designed FOV (50 μm and 500 μm along x axis and y axis, respectively) ensured the adequate response to the high-frequency ultrasounds (Fig. 2), enabling high-speed spectroscopic imaging in the OR-PAM system.

Representative PAM images captured at different times (Fig. 6(b)) gave the partial view of the phantom, which allows for reconstructing the whole structure (Fig. 6(c)) by stitching these fragmental visualizations together. After implementing the Fourier transformation and spectral calibration to the measured PA signals, the acoustic spectra of the segmental phantom are exhibited in Fig. 6(d), where the PA spectral band (i.e., center frequency, -6.0-dB spectral band, and -12.0-dB spectral band) is quantified over time. The broad bandwidth of our SPR sensor (Figs. 2 and 3(c)) can respond the phantom's PA impulses with the frequency components larger than ~120 MHz at -12.0-dB bandwidth. Furthermore, the PA spectra captured in the different snapshots fluctuated obviously (Fig. 6(d)). We attributed the visualizations to the fact that the imaged segments of the phantom (Fig. 6(b)) featured remarkable discrepancies in shape and orientation, leading to the laser-induced

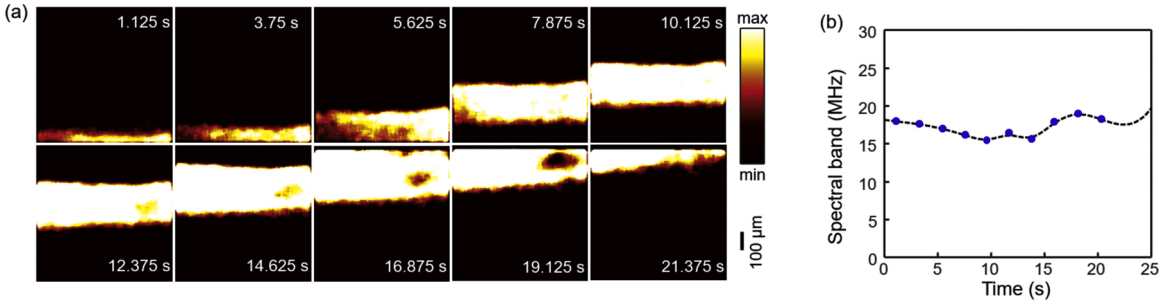

Fig. 5. (a) Snapshots of a moving black tape captured by our OR-PAM system. (b) PA spectra (-6.0-dB bandwidth) of the imaged black tape over time, in which the time point in the horizontal ordinate represents the intermediate time value of each snapshot.

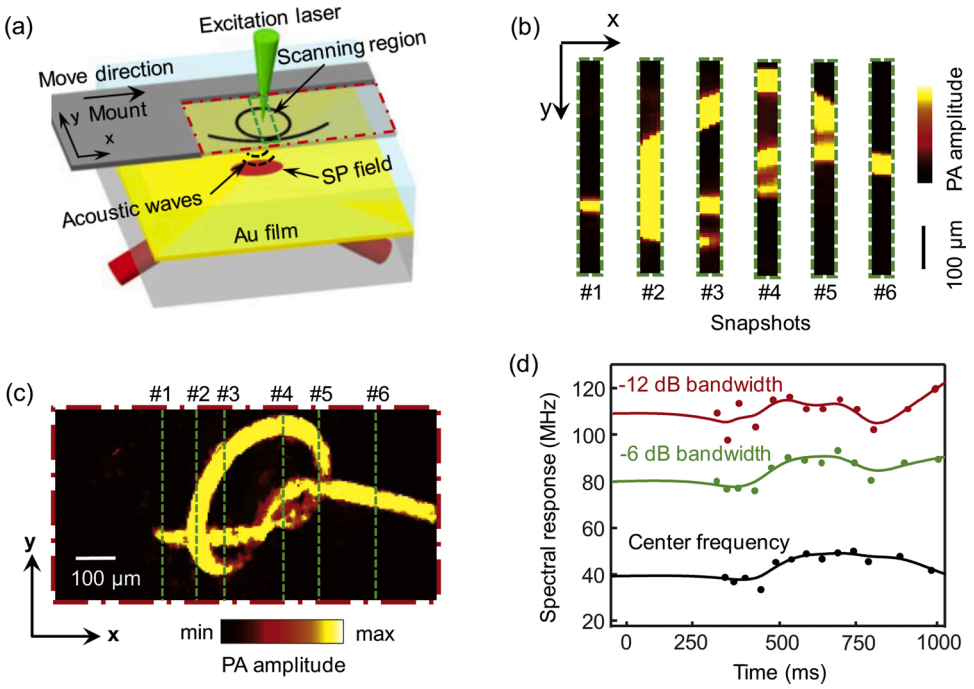

Fig. 6. Spectroscopic PAM imaging of a moving phantom made from the tungsten filament knot. (a) The schematic illustrates the operation mechanism for high-speed imaging of the sample. (b) Representative series of MAP images display the visualizations of the segmental phantom. (c) PAM image of the whole phantom that is stitched from the segmental images (b). The green dotted lines approximately point out the corresponding positions of the segmental MAP images (b). (d) Characteristics of the PA spectra over time, in which the time point in the horizontal ordinate represents the intermediate time value of each snapshot.

PA impulses encoding the complicated frequency components that were closely associated with both structure and scale [22–25]. Obviously, the PA signals of the tungsten filament knot characterized by more diverse acoustic spectra compared with the black tape with a relatively homogeneous structure. This implies that our system can obtain the PA spectroscopic analysis of the samples in addition to the high-speed morphological imaging.

3.4. *Spectroscopic PA imaging of a zebrafish eye ex vivo*

Zebrafish, having high genomic similarity with humans, is considered to be an ideal animal model in biology and diseases researches [48, 49]. To demonstrate the capability of our system for fast morphological imaging and broadband PA spectroscopic analysis of biological tissue, we performed PA imaging of an eye *ex vivo* from ~7 day-post

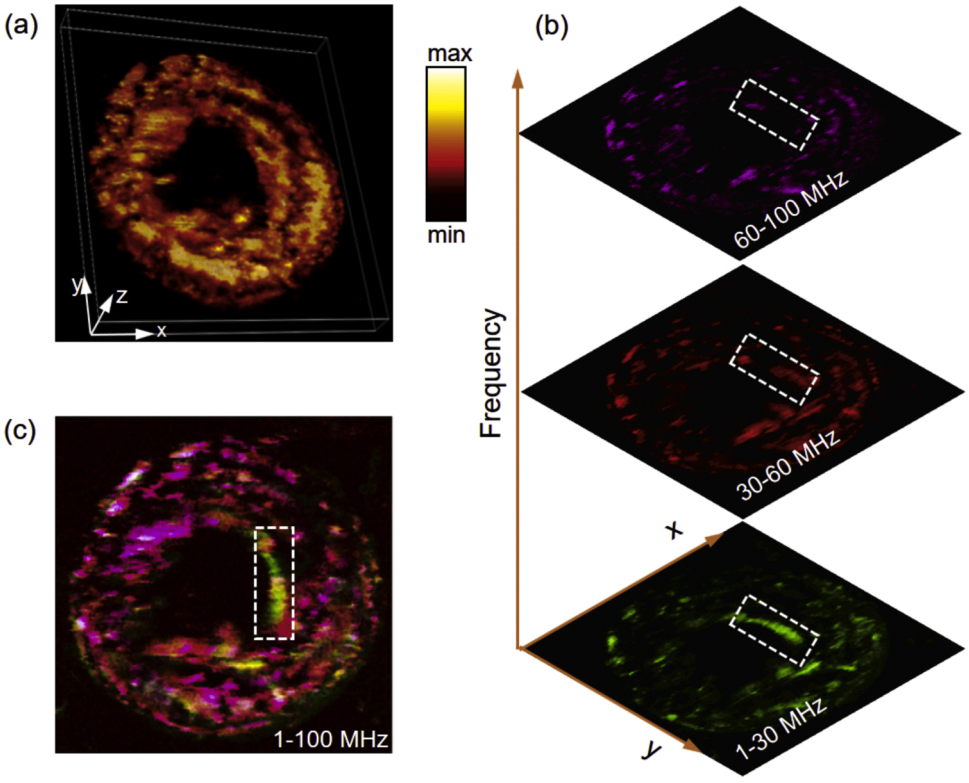

Fig. 7. Fast spectroscopic PA imaging of a zebrafish eye ex vivo. (a) The volumetric imaging of a zebrafish eye. (b) Color-coded PAM images reconstructed from the low- (~1-30 MHz), middle- (~30-60), and high-frequency bands (~60-100 MHz), respectively. (c) Superposed image of full bandwidth (1-100 MHz).

fertilization zebrafish larva. The zebrafish larva was anesthetized by positioning it into ~0.2 % tricaine and then euthanized by transferring it in ice water for 15 min before the dissection. The eye of the zebrafish larva was carefully removed and transferred to a coverslip, which was covered by a drop of the molten agarose. After ~20 min at room temperature until the agarose solidified, the eye was sandwiched between the coverslip and the agarose. All animal procedures were performed in accordance with laboratory animal protocols approved by the Animal Studies Committee of the Shenzhen University.

Relying on the optical absorption of melanin, we obtained label-free volumetric imaging of the zebrafish eye, which took ~3 s for acquiring a FOV of ~600 μm (x) × 600 μm (y) consisting of 300 pixels (x) × 300 pixels (y). To achieve high signal-to-noise ratio (SNR), the energy of the PA illumination laser delivered to the specimen was ~500 nJ per pulse, which corresponds to ~17 mJ/cm^2 at the specimen surface.

From the volumetric view (Fig. 7(a)) of the zebrafish eye, the microstructures of the zebrafish eye were clearly visible. Further, the PA spectra, which was calculated from the Fourier transform to each time-resolved PA signal, was divided into three spectral bands (low-frequency: ~1−30 MHz; middle-frequency: ~30−60 MHz; high-frequency: ~60−100 MHz). By the inverse fast Fourier transform, the corresponding time-resolved PA signals were obtained, forming the frequency-dependent PAM images in Fig. 7(b). As the frequency increasing, the anatomic dimensions gradually decrease, exhibiting many finer structures. The superposed view from the three spectral bands (Fig. 7(c)) represents the similar morphological features with the volumetric visualization (Fig. 7(a)), which is primarily because both views were reconstructed from the whole spectral band. The PA image reconstructed from the frequency domain revealed the spectrally-encoded information, which otherwise is overlooked in the volumetric view (Fig. 7(a)). As shown in the white boxes in Fig. 7(b) and (c), the spectrally-resolved anatomic structures are visible. This indicates that our spectroscopic OR-PAM system is capable of identifying the micro-anatomical features with different dimensions and shapes that are closely associated with the acoustic frequency components [24].

4. Conclusion

In this work, we developed a high-speed spectroscopic OR-PAM system by inegrating our previously-established broadband SPR sensor with the fast galvanometer scanning, demonstrating the capabilities of high-speed imaging acquisition over a scanning range of ~0.5 mm with broad spectral response of ~120 MHz. This allowed the OR-PAM system for visualizing the moving phantoms and characterizing the PA spectra over time simultaneously. Further, spectrally-dependent microanatomic images of the zebrafish eye were obtained over a frequency range up to 100 MHz, which, otherwise, is overlooked in our previous reports [31, 32].

It remains challenging to image the specimens with small size or weak optical absorption (e.g., red blood cell or cell nucleus) *in vivo* due to the insufficient ultrasonic detection sensitivity of the SPR sensor (~480 Pa in Fig. 1(d)). One solution is to adopt the advanced sensing methods, such as plasmonic waveguide resonance [41], phase sensing [42], and plasmonic metamaterial [43]. With the improved sensitivity, *in vivo* imaging is potentially accessed with the fast imaging acquisition and accurate PA spectroscopic analysis, which thus facilitate the practical biomedical PA investigations [24]. Additionally, the PA excitation and ultrasonic detection are on opposite sides of the imaging target in current OR-PAM system, which can't image the complicated anatomic sites (e.g., eye and brain). This constraint can be overcome by configuring a miniature SPR sensor within the central cone of a reflective objective, which permits our OR-PAM operating at reflection mode [32]. Due to the directional response characteristics of the SPR sensor, the imaging SNR decreases as the FOV increases. Hybrid optical and mechanical scanning modality [50] could achieve an enlarged FOV with sufficient imaging contrast. In a real biological environment, the PA spectroscopic analysis could be accessed using the illumination laser at certain wavelength to suppress the background noises. Taking account of the sample dimensions, the target of interest can be identified by selectively extracting the characteristic acoustic frequency components of the targeted chromophore.

In summary, with broadband frequency response and fast imaging rate, our OR-PAM system can acquire the volumetric imaging at high speed, and simultaneously conduct the spectroscopic analysis to the samples. These results suggest the potentials of the high-speed spectroscopic system in many prospective biomedical applications [44–47], for example, dynamic monitoring of the tumor response to various treatments by PA volumetric visualization and spectrally-resolved discrimination.

Declaration of Competing Interest

The authors declare no conflicts of interest.

Acknowledgements

Guangdong Major Project of Basic and Applied Basic Research: 2020B0301030009; National Natural Science Foundation of China (NSFC): 91750205, 61875130; Science and Technology Innovation Commission of Shenzhen: KQTD20170330110444030, JCYJ20200109113808048, KQJSCX20180328093810594; Natural Science Foundation of Guangdong Province: 2016A030312010, 2018B030311048. X. Yuan appreciates the support given by the leading talents of Guangdong province: No. 00201505, and W. Song appreciates the support from Shenzhen University: No. 860-000002110434.

Appendix A. Supplementary data

Supplementary material related to this article can be found, in the online version, at doi:https://doi.org/10.1016/j.pacs.2021.100305.

References

[1] L.V. Wang, Multiscale photoacoustic microscopy and computed tomography, Nat. Photonics 3 (2009) 503–509.
[2] L.V. Wang, S. Hu, Photoacoustic tomography: in vivo imaging from organelles to organs, Science 335 (2012) 1458–1462.
[3] L.V. Wang, J. Yao, A practical guide to photoacoustic tomography in the life sciences, Nat. Methods 13 (2016) 627–638.
[4] J. Yao, K. Maslov, Y. Zhang, Y. Xia, L.V. Wang, Label-free oxygen-metabolic photoacoustic microscopy in vivo, J. Biomed. Opt. 16 (2011), 076003.
[5] W. Song, Q. Wei, W. Liu, T. Liu, J. Yi, N. Sheibani, A. Fawzi, R.A. Linsenmeier, S. Jiao, H.F. Zhang, A combined method to quantify the retinal metabolic rate of oxygen using photoacoustic ophthalmoscopy, Sci. Rep. 4 (2014) 6525.
[6] L.J. Rich, M. Seshadri, Photoacoustic imaging of vascular hemodynamics: validation with blood oxygenation level-dependent MR imaging, Radiology 275 (2015) 110–118.
[7] J. Yao, L. Wang, J.M. Yang, K. Maslov, T. Wong, L. Li, C.H. Huang, J. Zou, L. V. Wang, High-speed label-free functional photoacoustic microscopy of mouse brain in action, Nat. Methods 12 (2015) 407–410.
[8] L. Lan, Y.M. Li, T. Yang-Tran, Y. Jiang, Y.C. Cao, J.X. Cheng, Ultraefficient thermoacoustic conversion through a split ring resonator, Advanced photonics 2 (3) (2020), 036006-036006.
[9] W. Song, W. Liu, H.F. Zhang, Laser-scanning doppler photoacoustic microscopy based on temporal correlation, Appl. Phys. Lett. 102 (2013), 203501.
[10] E.M. Strohm, E.S. Bernd, M.C. Kolios, Probing red blood cell morphology using high-frequency photoacoustics, Biophys. J. 105 (2013) 59–67.
[11] G. Diot, S. Metz, A. Noske, E. Liapis, B. Schroeder, S.V. Ovsepian, R. Meier, E. Rummeny, V. Ntziachristos, Multispectral optoacoustic tomography (MSOT) of human breast cancer, Clin. Cancer Res. 23 (2017) 6912–6922.
[12] Y. Zhou, J. Chen, C. Liu, C. Liu, L. Wang, Single-shot linear dichroism optical-resolution photoacoustic microscopy, Photoacoustics. 16 (2019), 100148.
[13] C. Liu, J. Chen, Y. Zhang, J. Zhu, L. Wang, Five-wavelength optical-resolution photoacoustic microscopy of blood and lymphatic vessels, Advanced Photonics. 3 (1) (2021), 016002.
[14] J. Park, B. Park, T.Y. Kim, S. Jung, C. Kim, et al., Quadruple ultrasound, photoacoustic, optical coherence, and fluorescence fusion imaging with a transparent ultrasound transducer, Proc. Natl. Acad. Sci. 118 (11) (2021) e1920879118.

[15] W. Song, W. Zheng, R. Liu, R. Lin, H. Huang, X. Gong, S. Yang, R. Zhang, L. Song, Reflection-mode in vivo photoacoustic microscopy with subwavelength lateral resolution, Biomed. Opt. Express 5 (2014) 4235–4241.
[16] S. Hu, L.V. Wang, Optical-resolution photoacoustic microscopy: auscultation of biological systems at the cellular level, Biophys. 105 (2013) 841–847.
[17] Z. Xie, S. Jiao, H.F. Zhang, C.A. Puliafito, Laser-scanning optical-resolution photoacoustic microscopy, Opt. Lett. 34 (2009) 1771–1773.
[18] P.H. Tran, D.S. Mukai, M. Brenner, Z. Chen, In vivo endoscopic optical coherence tomography by use of a rotational microelectromechanical system probe, Opt. Lett. 29 (2004) 1236–1238.
[19] J.M. Zara, S. Yazdanfar, K.D. Rao, J.A. Izatt, S.W. Smith, Electrostatic micromachine scanning mirror for optical coherence tomography, Opt. Lett. 28 (2003) 628–630.
[20] J.B. Chen, Y.C. Zhang, L.Y. He, Y.Z. Liang, L.D. Wang, Wide-field polygon-scanning photoacoustic microscopy of oxygen saturation at 1-MHz A-line rate, Photoacoustics 20 (2020), 100195.
[21] Q. Zhou, S. Lau, D. Wu, K.K. Shung, Piezoelectric films for high frequency ultrasonic transducers in biomedical applications, Prog. Mater. Sci. 56 (2011) 139–174.
[22] E.M. Strohm, E.S. Bernd, M.C. Kolios, Probing red blood cell morphology using high-frequency photoacoustics, Biophys. J. 105 (2013) 59–67.
[23] G. Xu, Z.X. Meng, J.D. Lin, C.X. Deng, P.L. Carson, J.B. Fowlkes, C. Tao, X. Liu, X. Wang, High resolution physio-chemical tissue analysis: towards non-invasive in vivo biopsy, Sci. Rep. 6 (2016) 16937.
[24] G. Xu, J.B. Fowlkes, C. Tao, X.J. Liu, X.D. Wang, Photoacoustic spectrum analysis for microstructure characterization in biological tissue: analytical model, Ultrasound Med. Biol. 41 (2015) 1473–1480.
[25] H. Li, B. Dong, Z. Zhang, H.F. Zhang, C. Sun, A transparent broadband ultrasonic detector based on an optical micro-ring resonator for photoacoustic microscopy, Sci. Rep. 4 (2014) 4496.
[26] C. Zhang, T. Ling, S. Chen, L.J. Guo, Ultrabroad bandwidth and highly sensitive optical ultrasonic detector for photoacoustic imaging, ACS Photonics 1 (2014) 1093–1098.
[27] A.P. Jathoul, J. Laufer, O. Ogunlade, B. Treeby, B. Cox, E. Zhang, P. Johnson, A. R. Pizzey, B. Philip, T. Marafioti, M.F. Lythgoe, R.B. Pedley, M.A. Pule, P. Beard, Deep in vivo photoacoustic imaging of mammalian tissues using a tyrosinase-based genetic reporter, Nat. Photonics 9 (2015) 239–246.
[28] T. Wang, R. Cao, B. Ning, A.J. Dixon, J.A. Hossack, A.L. Klibanov, Q. Zhou, A. Wang, S. Hu, All-optical photoacoustic microscopy based on plasmonic detection of broadband ultrasound, Appl. Phys. Lett. 107 (2015), 153702.
[29] X. Zhu, Z. Huang, G. Wang, W. Li, D. Zou, C. Li, Ultrasonic detection based on polarization-dependent optical reflection, Opt. Lett. 42 (2017) 439.
[30] F. Yang, W. Song, C. Zhang, C. Min, H. Fang, L. Du, P. Wu, W. Zheng, C. Li, S. Zhu, X. Yuan, Broadband graphene-based photoacoustic microscopy with high sensitivity, Nanoscale. 10 (2018) 8606–8614.
[31] W. Song, G. Guo, J. Wang, Y. Zhu, C. Zhang, H. Fang, C. Min, S. Zhu, X. Yuan, In vivo reflection-mode photoacoustic microscopy enhanced by plasmonic sensing with an acoustic cavity, ACS Sens. (25) (2019) 2697–2705.
[32] W. Song, L. Peng, G. Guo, F. Yang, Y. Zhu, C. Zhang, C. Min, H. Fang, S. Zhu, X. Yuan, Isometrically resolved photoacoustic microscopy based on broadband surface plasmon resonance ultrasound sensing, ACS Appl. Mater. Interfaces 31 (2019) 27378–27385.
[33] C. Min, Z. Shen, J. Shen, Y. Zhang, H. Fang, G. Yuan, L. Du, S. Zhu, T. Lei, X. Yuan, Focused plasmonic trapping of metallic particles, Nat. Commun. 4 (2013) 2891.
[34] R. Nuster, G. Paltauf, P. Burgholzer, Comparison of surface plasmon resonance devices for acoustic wave detection in liquid, Opt. Express 15 (2007) 6087.
[35] Z. Zhang, B. Dong, H. Li, F. Zhou, H. Zhang, C. Sun, Theoretical and experimental studies of distance dependent response of micro-ring resonator-based ultrasonic detectors for photoacoustic microscopy, J. Appl. Phys. 14 (2014) 175.
[36] W. Song, S. Xiao, C. Min, H. Fang, X. Yuan, Theoretical and experimental studies on broadband photoacoustic response of surface plasmon sensing, Appl. Phys. Lett. 116 (2020), 243504.
[37] L.V. Wang, Photoacoustic Imaging and Spectroscopy, CRC Press, 2009.
[38] M. Xu, L.V. Wang, Photoacoustic imaging in biomedicine, Rev. Sci. Instrum. 77 (2006), 041101.
[39] H. Li, B. Dong, Z. Zhang, H.F. Zhang, C. Sun, A transparent broadband ultrasonic detector based on an optical micro-ring resonator for photoacoustic microscopy, Sci. Rep. 4 (2014) 4496.
[40] C. Zhang, T. Ling, S. Chen, L.J. Guo, Ultrabroad bandwidth and highly sensitive optical ultrasonic detector for photoacoustic imaging, ACS Photonics 1 (2014) 1093–1098.
[41] P. Zhang, L. Liu, Y. He, X. Chen, K. Ma, D. Wei, H. Wang, Q. Shao, Composite layer based plasmon waveguide resonance for label-free biosensing with high figure of merit, Sens. Actuators B Chem. 272 (2018) 69–78.
[42] R. Shnaiderman, G. Wissmeyer, M. Seeger, D. Soliman, H. Estrada, D. Razansky, A. Rosenthal, V. Ntziachristos, Fiber interferometer for hybrid optical and optoacoustic intravital microscopy, Optica. 4 (2017) 1180–1187.
[43] Z. Fang, X. Zhu, Plasmonics in nanostructures, Adv. Mater. 25 (2013) 3840.
[44] M.J. Moore, E.M. Strohm, M.C. Kolios, Assessment of the nucleus-tocytoplasmic ratio in MCF-7 cells using ultra-high frequency ultrasound and photoacoustics, Int. J. Thermophys. 37 (2016) 1–10.
[45] E.M. Strohm, M.C. Kolios, Classification of blood cells and tumor cells using label-free ultrasound and photoacoustics, Cytometry A. 87 (2015) 741–749.
[46] E. Hysi, L.A. Wirtzfeld, J.P. May, E. Undzys, S.D. Li, M.C. Kolios, Photoacoustic signal characterization of cancer treatment response: correlation with changes in tumor oxygenation, Photoacoustics. 5 (2017) 25.
[47] E. Hysi, R.K. Saha, M.C. Kolios, Photoacoustic ultrasound spectroscopy for assessing red blood cell aggregation and oxygenation, J. Biomed. Opt. 17 (2012), 1250061.
[48] J.T. Shin, M.C. Fishman, From zebrafish to human: modular medical models, Annu. Rev. Genomics Hum. Genet. 3 (2002), 311-311.
[49] G.J. Lieschke, P.D. Currie, Animal models of human disease: zebrafish swim into view, Nat. Rev. Genet. 8 (2007) 353–367.
[50] L. Li, C. Yeh, S. Hu, L. Wang, B.T. Soetikno, R. Chen, Q. Zhou, K.K. Shung, K. I. Maslov, L.V. Wang, Fully motorized optical-resolution photoacoustic microscopy, Opt. Lett. 7 (2014) 2117–2120, 39.

Fan Yang is a pH.D student at College of Physics and Optoelectronic Engineering, Shenzhen University, Shenzhen, China. He received Bachelor degree from the Hebei University of Science and Technology, and received M.S. degree from Shenzhen University. His research focuses on the development of novel photoacoustic imaging technologies.

Guangdi Guo received the M.S. degree from Shenzhen University, Shenzhen, China, in 2020. His research interests include optical sensing and photoacoustic imaging.

Shanguang Zheng received the M.S. degree from Shenzhen University, Shenzhen, China, in 2018. His research interests include optical vortices and applications.

Hui Fang is currently a professor in Nanophotonics Research Center, Institute of Microscale Optoelectronics, Shenzhen University. His research interests include photoacoustic imaging and flow sensing, optical microscopy and spectroscopy, and optical vector beams.

Changjun Min received his B.S. degree and pH.D. degree from University of Science and Technology of China in 2003 and 2008, respectively. During 2008–2011 he was a postdoctoral research fellow in Louisiana State University (USA) and then in Nanyang Technological University (Singapore). During 2011–2014, he worked as Associate Professor in Nankai University (China). Since June 2014, he joined the College of Optoelectronic Engineering in Shenzhen University (China). His research interests include plasmonics, optical sensing/imaging, optical tweezers, vector beams, and metasurface. He has published over 100 journal papers in optics and photonics.

Wei Song received his pH.D. degree from Harbin Institute of Technology, Harbin, China, in 2014. He was an assistant professor with Shenzhen Institute of Advanced Technology from 2015 to 2016. Since 2017, he works as an assistant professor at Nanophotonics Research Centre, Shenzhen University. His main interest is the development and application of novel optical sensing and imaging technologies, including optical surface wave sensing, photoacoustic microscopy, and multimodal imaging.

X.-C. Yuan received BEng and MEng degrees in Optical Engineering from Tianjin University, China, in 1985 and 1988, respectively, and pH.D. degree in Physics from the University of London, King's College, in 1994. Between 1994 and 1999, he was a research fellow with the Cavendish Laboratory, the University of Cambridge. Between 1999 and 2008, he was a faculty (tenured) in the School of EEE of Nanyang Technological University, Singapore. He joined the Institute of Modern Optics of Nankai University as a Chang Jiang distinguished professor in 2008. He relocated to Shenzhen University in 2013 to found the Nanophotonics Research Centre. His current work deals with optical vortices and applications, optical trapping, plasmonics in microscopy, and optical communication with orbital angular momentum. He has published more than 250 journal papers in optics and photonics. He is a SPIE and OSA Fellow.